
Two-Dimensional Simulations of the Neutron Yield in Cryogenic-DT Implosions on OMEGA

Introduction

Inertial confinement fusion (ICF) has been actively pursued for decades¹ since it was proposed in the early 1970s (Ref. 2). In the so-called “hot-spot” ignition designs, a capsule containing a cryogenic deuterium–tritium (DT) ice layer and low-density DT gases is imploded directly by intense laser pulses³ or indirectly by x rays in a hohlraum.⁴ The ultimate goal of ICF is to ignite the imploding target, producing net energy gain. To reach this goal, the cryogenic-DT shell must be sufficiently low in temperature that it can be compressed to an extremely high density ($>1000\times$ solid-DT density), resulting in an areal density ($\rho R \geq 1 \text{ g/cm}^2$) to provide sufficient inertial confinements for burn-wave propagation. The temperature in the hot spot must be sufficiently high so that the resulting fusion α particles can “trigger” the burn-wave propagation for ignition. Both conditions are necessary for the success of hot-spot ICF ignition. Nonuniformities seeded by target and laser perturbations grow exponentially via Rayleigh–Taylor (RT) instability⁵ during the acceleration and deceleration of the fuel shell. This perturbation growth can disrupt the neutron yield (α -particle production) from the core through cooling the hot spot by either injecting “cold” material into the core or increasing heat flow out of the hot spot because of the increased surface area. This reduces the effective hot-spot volume, density, and temperature.⁶ The yield-over-clean (YOC), defined as the ratio of experimental neutron yield to its value from one-dimensional (1-D) simulations, is conventionally used to describe the neutron-yield reduction caused by perturbations. It has been shown⁷ that a minimum YOC requirement ($\text{YOC}_{\min} \geq 40\%$ to 50%) must be met at the National Ignition Facility (NIF)⁸ for both direct- and indirect-drive–ignition designs to be successful. By scaling the hydro-equivalent NIF-ignition designs to OMEGA, it has been suggested that the YOC of cryogenic-DT implosions on OMEGA should be $\sim 15\%$ to 20% (Ref. 7) to have confidence that a scaled NIF target will ignite.

Over the past years RT growth of various perturbations has been extensively studied for both planar and spherical targets through theoretical analyses/simulations⁹ and experiments.^{10–14} These perturbations include the target offset from

target chamber center, the ice roughness of the cryogenic-DT layer, and the laser nonuniformities. Understanding the effects of each of the perturbation sources and their combination on the neutron-yield reduction through multidimensional simulations compared with experiments is critical to identifying the major nonuniformity sources that should be improved. For ICF ignition designs, the perturbation growth generally depends on the target design and laser pulse shapes. A comprehensive study of cryogenic deuterium (D_2) implosions on OMEGA¹⁵ has been presented in Ref. 16. As opposed to the cryogenic- D_2 , continuous-pulse implosions, the high-compression [$\langle \rho R \rangle > 200 \text{ mg/cm}^2$] cryogenic-DT implosions are driven by triple-picket designs with a higher convergence ratio and small hot spot. This article is devoted to a thorough understanding of the neutron-yield performance in cryogenic-DT implosions on OMEGA.^{17,18} Two-dimensional (2-D) *DRACO*¹⁹ simulations have been performed to systematically investigate each of the perturbation sources and their combined effects on the neutron yield. The *DRACO* simulations reproduced the trends observed in experiments. The simulated YOC’s agree with the experimental YOC within a factor of 2 or better, and the simulated neutron-averaged ion temperatures agree with measurements within the experimental uncertainty. Major nonuniformity sources are identified for the triple-picket plus step-pulse designs:^{17,18} the target offset with respect to the target chamber center and laser imprinting. This is in contrast to the cryogenic- D_2 implosions¹⁶ where the ice-layer roughness is much more dominant. The simulations of DT implosions suggest that to increase YOC from the current level of $\sim 5\%$ to the hydro-equivalent ignition level of $\sim 15\%$ to 20% (maintaining $\langle \rho R \rangle = 200$ to 300 mg/cm^2), the target offset must be less than $\sim 10 \mu\text{m}$ and smoothing by spectral dispersion (SSD) must be applied.

The following sections (1) briefly describe the experiments and the basics of 2-D radiation–hydrodynamic simulations for cryogenic-DT implosions, respectively; (2) describe the detailed simulation results that examine each of the nonuniformity sources and their combined perturbation effects on the neutron-yield reduction; (3) discuss the integrated *DRACO* simulations

for individual cryogenic-DT shots by including the actual target and laser nonuniformities in experiments; (4) compare the simulated YOC and the neutron-averaged ion temperature with experiments; and (5) formulate the relationship between YOC and the temperature-over-clean (TOC), indicating how much distortion occurs in the hot-spot formation. Conclusions are presented in the last section.

Experiments of Cryogenic-DT Implosions on OMEGA

Low-adiabat ($\alpha \sim 2.0$ to 2.5, which is conventionally defined as the ratio of DT-fuel pressure to the Fermi-degenerate pressure), cryogenic-DT implosion experiments have been conducted on OMEGA with the multiple-picket drive pulses^{17,18} shown in Figs. 123.1(a) and 123.1(b). The targets, shown in Fig. 123.1(c), were energy scaled from the ignition design on the National Ignition Facility (NIF).¹⁷ The OMEGA target had an 860- μm diameter, with an $\sim 10\text{-}\mu\text{m}$ plastic (CD) ablator filled with approximately 650 atm of DT (nominally 50:50) gas at standard temperature and pressure. When cooled to the triple point (approximately 18.7 K), a DT-ice layer ($\sim 65\ \mu\text{m}$ thick) formed inside the shell. The targets were mounted on 17- μm -diam SiC stalks. The triple-picket design^{17,18} is motivated by the desire to precisely tune the multiple shock waves to maintain a low-implosion adiabat and to minimize shock preheating of the fuel. The pickets launch a series of decaying shocks that are designed to coalesce nearly simultaneously with the main shock near the inner surface of the cold fuel. Shock-timing measurements in liquid deuterium with a velocity interferometer system for any reflector (VISAR)²⁰ are used to obtain a laser pulse shape that places the DT fuel on the desired adiabat. By adjusting the picket energies, low-adiabat ($\alpha \sim 2$), high-compression [$\langle \rho R \rangle_n \sim 300 \pm 47\ \text{mg/cm}^2$ inferred by a magnetic recoil spectrometer (MRS)²¹] implosions have been demonstrated on OMEGA.^{17,18}

For the OMEGA cryogenic-DT experiments, both the triple-picket (TP) plus square main pulse [Fig. 123.1(a)] and triple-picket plus step main pulse [Fig. 123.1(b)] have been used to drive target implosions. The former design resulted in an in-flight adiabat of $\alpha \sim 2.5$ and a convergence ratio of $C_R \sim 19$, while the step main pulse drove a lower-adiabat ($\alpha \sim 2.0$) implosion with a higher convergence ratio of $C_R \sim 24$ (resulting in higher $\langle \rho R \rangle$). The total laser energy was 23 kJ for the square main pulse and 25 kJ for the step main pulse. With a peak intensity of $\sim 8 \times 10^{14}\ \text{W/cm}^2$, the predicted implosion velocity in these designs is $v_{\text{imp}} = 3 \times 10^7\ \text{cm/s}$. Details of the compression dynamics, the areal-density (ρR) measurement, and the triple-picket ignition design for the NIF can be found in Refs. 17 and 18.

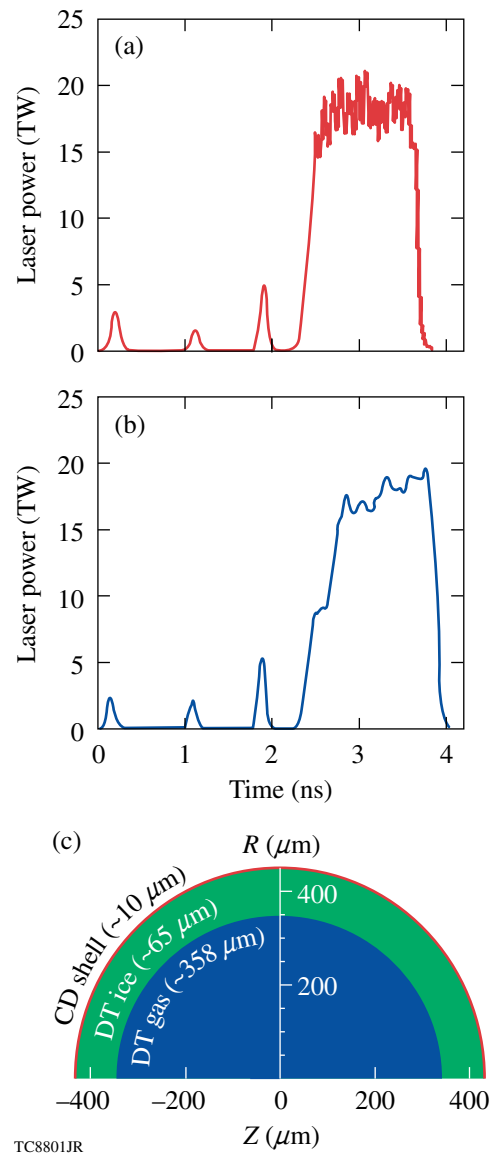


Figure 123.1

(a) The triple-picket plus square main pulse and (b) the triple-picket plus step main pulse used for cryogenic-DT implosions on the OMEGA laser. (c) A schematic diagram of a cryogenic-DT target.

The neutron yields from DT fusion were measured with a combination of activation, scintillation, and track recorder detectors. The yield of these implosions, 1×10^{12} to 6×10^{12} neutrons, varied from $\sim 3\%$ to $\sim 10\%$ of the 1-D hydrodynamic simulation prediction, depending on the pulse shape, target offset, ice roughness, and beam smoothing. The neutron-averaged ion temperature ($\langle T_i \rangle_n$) was inferred using neutron time-of-flight spectroscopy.²² The accuracy of these measurements was approximately $\pm 0.5\ \text{keV}$, depending on the measurement

configuration and the neutron-hit statistics in the detectors. Improvements to reduce the error bar in $\langle T_i \rangle_n$ measurements are underway. The measured $\langle T_i \rangle_n$ and the absolute neutron yields are lower than the 1-D–predicted values, as a consequence of laser and target perturbations including ice roughness, laser-drive nonuniformity (primarily pointing- and single-beam nonuniformity), capsule-surface imperfections associated with the stalk mount, and target offsets from the locus of laser-beam pointing. The subsequent sections provide a systematic investigation of how these nonuniformities reduce the neutron yield and the ion temperature in the hot spot. The simulations are used to identify the major perturbation sources and to suggest possible improvements for the implosion-yield performance.

Two-Dimensional DRACO Simulations

To understand the various laser and target perturbation effects on the cryogenic-DT implosion experiments, multi-dimensional hydrodynamic simulations were performed. The two-dimensional, radiation hydrodynamics code *DRACO* has been developed at LLE for both implosion and planar-target simulations.¹⁹ For spherical implosion simulations, the *DRACO* coordinates are defined by the cylindrical axis \mathbf{Z} and the radius \mathbf{R} , with the assumption of azimuthal symmetry. This study used *DRACO*'s Lagrangian version. Laser absorption in the plasma corona by inverse bremsstrahlung was modeled by three-dimensional (3-D) ray tracing with OMEGA's port geometry.²³ The equation-of-state (EOS) of materials was determined from the *SESAME* EOS table.²⁴ The radiation transport in *DRACO* used the multigroup diffusion model, in which the Astrophysics Opacity Table (AOT)²⁵ is applied.

In direct-drive ICF implosions, the laser energy absorbed near the critical-density region is thermally transported to the ablation surface mainly by electrons. The thermal-transport model in direct-drive ICF is crucial for properly simulating the target drive. Flux-limited Spitzer thermal conductivity is often used in laser-plasma fluid modeling.²⁶ The standard flux limiter $f = 0.06$ was used in the 2-D simulations. Previous experiments with planar and spherical targets^{27–29} have shown that this flux limiter works well for the laser intensities used here. The 1-D simulations of the cryogenic-DT implosions were modeled using both classical (flux-limited) heat transport and a nonlocal heat-transport model³⁰ and were found to be insensitive to the transport model.

A series of planar and spherical experiments were conducted to benchmark the *DRACO* simulations.^{11–14,16,19,29,31,32} The code capability of simulating the Rayleigh–Taylor instability growth has been demonstrated with intense laser-driven planar/

spherical target experiments on OMEGA.^{11–14} The RT growth of perturbations either by pre-imposed mass modulation^{11,12} or by direct laser imprinting^{13,14} has been properly predicted by *DRACO* simulations. A systematic study of the neutron yield in cryogenic-D₂ implosions on OMEGA was performed with 2-D *DRACO* simulations.¹⁶ The simulation results generally reproduced the experimental trend in YOC versus target offset and ice roughness for 5- μm -thick CD-shell targets, while for 10- μm -thick CD-shell targets, laser imprinting reduced the yield by a factor of 2. Following our previous experience in simulating cryogenic-D₂ implosions, cryogenic-DT implosions are systematically investigated for each of the perturbation sources and their combined effects on the yield performance. Comparing simulations with experiments elucidates the major perturbations and suggests how to increase the neutron yield in the experiments.

Simulation Results for Various Laser and Target Perturbations

In cryogenic-DT experiments, a variety of laser and target perturbations determine the implosion performance. Two kinds of laser perturbations will be addressed: (a) long-wavelength beam-to-beam perturbations ($\ell < 20$) such as mistiming, mispointing, and power imbalance among beams and (b) single-beam laser imprinting in the high-mode regime (up to $\ell \sim 200$). The target perturbations include the target offset from the target chamber center and the inner surface roughness of the ice layer. In this section, each of the nonuniformity sources will be investigated separately and their combined effect on yield performance will be examined.

1. Long-Wavelength Laser Nonuniformities

The 60-beam OMEGA Laser Facility¹⁵ can deliver up to 30-kJ, 351-nm UV energies on target. Each laser beam, coming from ports in a 3-D geometry, is equipped with a super-Gaussian (SG-4) phase plate³³ and polarization smoothing³⁴ is employed. The low-mode (long-wavelength) perturbation effects include the power imbalance (PIB) among beams, the beam-to-beam mistiming (MT), and the static mispointing (MP) of each beam. Their effects have been investigated separately with *DRACO* simulations of cryogenic-DT target performance using different levels of perturbation σ_{rms} . The results are summarized in Tables 123.I–123.III. A normal distribution of random perturbation amplitudes from each laser beam is assumed for a given σ_{rms} . For example, Table 123.I shows that for the square main pulse, the YOC decreases from 94.1% to 81.1% as the mistiming changes from $\sigma_{\text{rms}} = 9$ ps to $\sigma_{\text{rms}} = 40$ ps. Table 123.II shows that a static mispointing of $\sigma_{\text{rms}} = 50$ μm reduces the YOC to 65%. For power imbalance

among the beams, the pickets' power imbalance is more important than the main drive pulse because the PIB nonuniformity can be more efficiently seeded during the pickets. As shown in Table 123.III, a PIB of $\sigma_{\text{rms}} = 10\%$ during the pickets can reduce the YOC to 74%, even when the main pulse's PIB is $\sigma_{\text{rms}} = 3\%$. This level of PIB during the pickets has been seen in cryogenic-DT experiments. The PIB in cryogenic-DT pulse shapes has recently been improved to an overall $\sigma_{\text{rms}} = 3\%$ to 4%, which recovers the YOC to a level of $\sim 90\%$.

Table 123.I: YOC dependence on beam-to-beam mistiming for the square main pulse.

Beam-to-beam mistiming	YOC (%)
$\sigma_{\text{rms}} = 9$ ps	94.1
$\sigma_{\text{rms}} = 25$ ps	90.4
$\sigma_{\text{rms}} = 40$ ps	81.1

Table 123.II: YOC dependence on beam mispointing for the step main pulse.

Static beam mispointing	YOC (%)
$\sigma_{\text{rms}} = 10$ μm	91.9
$\sigma_{\text{rms}} = 30$ μm	77.0
$\sigma_{\text{rms}} = 50$ μm	65.0

Table 123.III: YOC dependence on beam-power imbalance for the step main pulse.

Beam-power imbalance	YOC (%)
$\sigma_{\text{rms}} = 3\%$ (pickets) and 3% (main pulse)	92.9
$\sigma_{\text{rms}} = 3\%$ (pickets) and 10% (main pulse)	90.3
$\sigma_{\text{rms}} = 10\%$ (pickets) and 3% (main pulse)	74.0

By using a nominal laser perturbation level for each source on OMEGA, the simulation results of their combined effects on the cryogenic-DT yield performance are listed in Table 123.IV for both pulse shapes. The combined effects of the three nominal perturbations (MT: $\sigma_{\text{rms}} = 9$ ps; MP: $\sigma_{\text{rms}} = 10$ μm ; PIB: $\sigma_{\text{rms}} = 3\%$ overall) reduce the yield by $\sim 7\%$ for the square main pulse and by $\sim 17\%$ for the step main pulse. The latter is more sensitive to perturbations since it drives a lower-adiabat, high-convergence implosion. In the following sections, these nominal low- ℓ -mode laser nonuniformities have been included since they are always present in OMEGA experiments.

2. Target Offset

The target can be offset from the target chamber center as a result of vibration when the cryogenic shroud is retracted. It is measured at shot time using time-integrated x-ray pinhole cameras. As shown in cryogenic-D₂ implosions,¹⁶ the target offset imposes a dominant $\ell = 1$ perturbation. This is due to the asymmetry of laser illumination on the target, which results in less laser absorption in the offset direction. As a result, the shock breaks out asymmetrically and the overdriven side converges more and achieves a higher density. The uneven drive compresses the target asymmetrically, reducing the final hot-spot volume, temperature, and density. The density contours for the square-main-pulse design are plotted in Figs. 123.2(a) and 123.2(b) at peak compression for the cases of 20- μm and 40- μm offsets from the target chamber center. The corresponding ion-temperature contour plots are shown in Figs. 123.2(c) and 123.2(d). As the target offset increased, the compression asymmetry increased; the ion temperature and effective volume for neutron production in the hot spot were reduced, leading to a reduction in neutron yield. The target offsets of 20 μm and 40 μm caused the YOC to decrease to 72% and 36.4%, respectively.

Carrying out *DRACO* simulations for different target offsets, the YOC was plotted as a function of target offset in Fig. 123.3 for both the square main pulse (red circles) and the step main

Table 123.IV: YOC degradation caused by the smallest low-mode beam perturbations on OMEGA.

Smallest OMEGA beam nonuniformities	YOC (%)	YOC (%)
	(square main pulse)	(step main pulse)
Mistiming ($\sigma_{\text{rms}} \sim 9$ ps)	94.1	92.2
Mispointing ($\sigma_{\text{rms}} \sim 10$ μm)	93.8	91.9
Power imbalance ($\sigma_{\text{rms}} \sim 3\%$ overall)	93.6	92.9
All above perturbations together	93.4	83.3

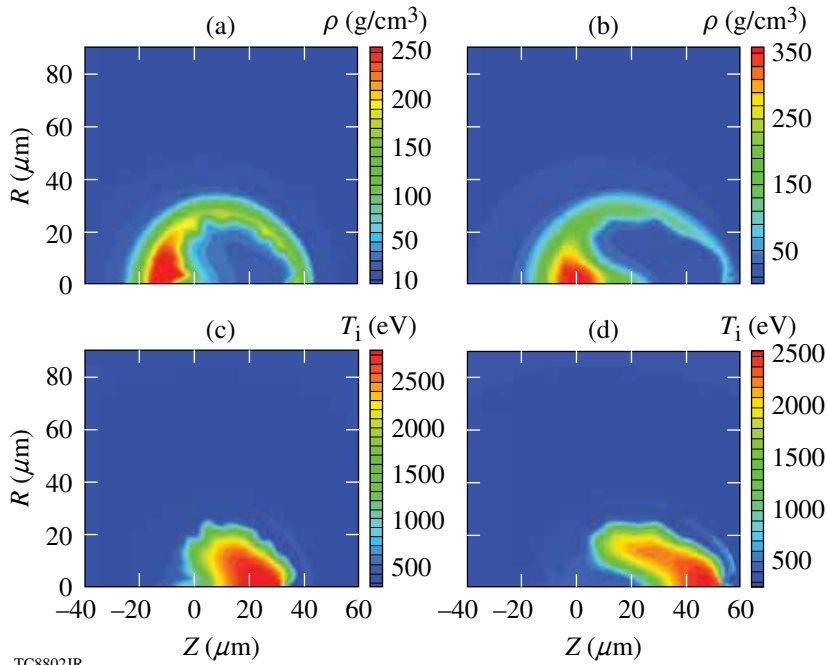


Figure 123.2
The density contour plots at peak compression for target offsets of (a) 20 μm and (b) 40 μm from the target chamber center, for the square-main-pulse case. The corresponding ion temperatures are shown in (c) and (d), respectively.

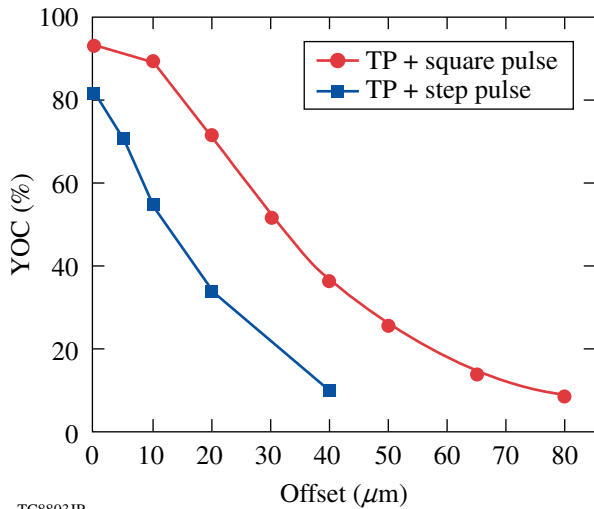


Figure 123.3
The YOC is plotted as a function of target offset for the two types of pulses shown in Figs. 123.1(a) and 123.1(b).

pulse (blue squares). The step main pulse is more sensitive to the target offset than the square main pulse. For example, at 20- μm offset the YOC is $\sim 72\%$ for the square main pulse, while it is $\sim 34\%$ for the step-main-pulse design. This factor of ~ 2 reduction is consistent with the experimental observations for these two pulse shapes (see **DRACO Simulations of Individual Cryogenic-DT Shots**, p. 122). The dominant $\ell = 1$ perturbation has been confirmed by experimental ρR

measurements. As shown in Fig. 123.2(b), if the ρR detector is sitting along the $+z$ axis (along the target offset), it measures the smallest ρR ; while, if it sits on the $-z$ axis (against the target offset), it will measure the largest ρR . Indeed, two shots with large offsets (35 μm and 39 μm) have shown such asymmetric ρR results [$\langle \rho R \rangle_{\text{CPS}_1} = 50 \text{ mg/cm}^2$ and $\langle \rho R \rangle_{\text{CPS}_2} = 180 \text{ mg/cm}^2$], experimentally inferred from the knock-on-deuteron (KOD) spectrum following elastic (n,D) scattering.³⁵ For these two shots, the two charged-particle spectrometers (CPS₁ and CPS₂) were roughly in line with the direction of target offset. The shape of the KOD spectrum evolves dramatically as the fuel areal density increases up to 180 mg/cm^2 ; above 180 mg/cm^2 , the shape of the spectrum no longer changes with increasing areal density and the measurement is saturated.³⁵

3. Ice Roughness

For the cryogenic-DT targets imploded on OMEGA, 10- μm CD shells were permeation filled with an equimolar mixture of DT to 650 atm. The shell and gas were then slowly cooled to just below the DT triple point (18.7 K). By controlling the exchange-gas pressure and the temperature of the copper-layering sphere, a spherical isotherm can be maintained at the ice surface inside the capsule, and β -layering produces high-quality layers.^{36,37} During formation of the ice layer, the inner ice surface was characterized using optical shadowgraphy.³⁸ A typical shadowgraph of a cryogenic-DT target is shown in Fig. 123.4(a); the inner-surface position is “unwrapped” azimuthally around the center of the capsule to form a line in

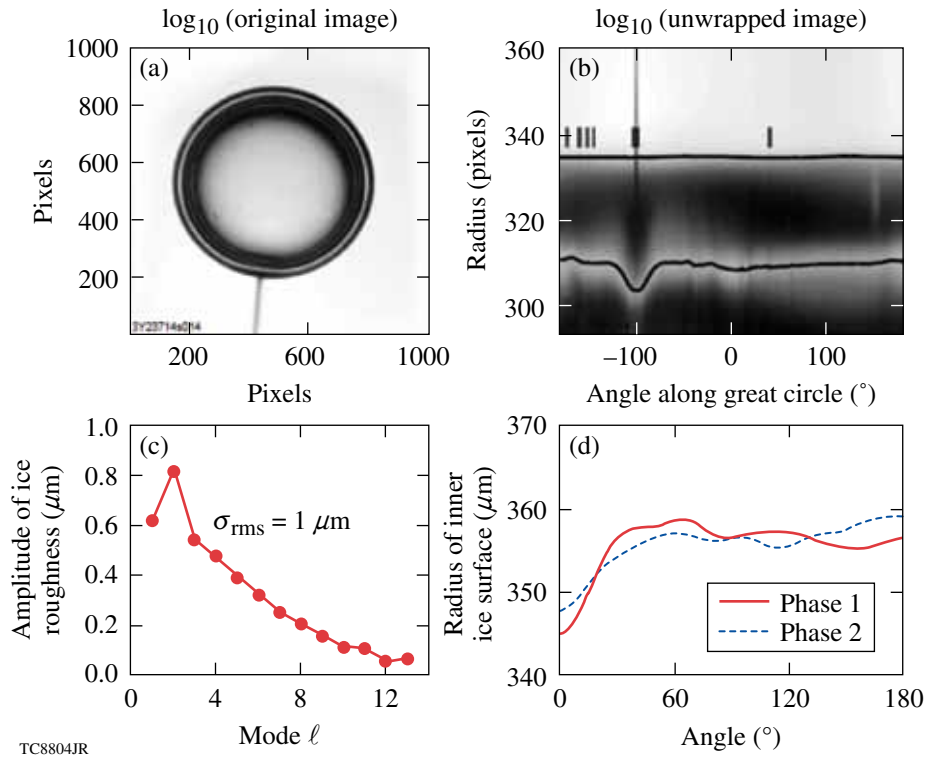


Figure 123.4

(a) A typical cryogenic-DT target view; (b) the ice-layer radius plotted versus angle; (c) a typical spectrum of ice roughness ($\sigma_{\text{rms}} = 1.0 \mu\text{m}$) at the inner surface (the thick part near the stalk has been excluded); (d) the angle-dependent radius of the inner ice surface for two different phases but same σ_{rms} , which were composed for our *DRACO* simulations.

radius–azimuth space [Fig. 123.4(b)]. Figure 123.4(c) shows the typical power spectrum of the ice roughness ($\sigma_{\text{rms}} = 1 \mu\text{m}$) as a function of the mode number, which was generated by fitting the Fourier amplitudes of the radial variation as a function of the azimuth.³⁹ Using the measured spectrum, the ice-layer thickness (ΔR) was composed for the *DRACO* simulations,

$$\Delta R(\theta) = \Delta R_0 + \sum_{\ell=1}^n \pm A_{\ell} \cos(\ell\theta), \quad (1)$$

where ΔR_0 is the average thickness of the ice layer and A_{ℓ} is the perturbation amplitude of the ℓ th mode. Because of the azimuthal symmetry imposed in 2-D *DRACO*, the phase among different modes must be either 0 or π , giving a plus (+) or minus (−) sign in the superposition of each mode. Different combinations of these signs provide various “phases” of the ice layer, which give different perturbed shell thicknesses along the polar angle θ , even though σ_{rms} is the same. The inner-surface radius as a function of angle has been plotted in Fig. 123.4(d) for two such phases, respectively, by solid (red) and dashed (blue) lines. The “dips” in radius around the stalk were modeled with the superposition of a Gaussian bump, around $\theta = 0^\circ$.

Different phases of ice roughness can vary the target-yield performance. Examples are shown in Figs. 123.5(a) and 123.5(b) for density contours at peak compression for phase 1 and phase 2 [shown in Fig. 123.4(d)], respectively, at $\sigma_{\text{rms}} = 1.0 \mu\text{m}$ with the step main pulse. The simulations show a neutron yield of $\text{YOC} = 78\%$ for phase 1 and $\text{YOC} = 56\%$ for phase 2. The “ice bump” around the stalk has not yet been included in the ice-roughness-only studies but will be included in the individual shot simulations. Considering only the ice roughness (without the localized ice bump), Fig. 123.5(c) shows the YOC as a function of ice roughness σ_{rms} from *DRACO* simulations for both $\sigma_{\text{rms}} = 1.0 \mu\text{m}$ and $\sigma_{\text{rms}} = 3.0 \mu\text{m}$ with three random phases. The error bar for each case represents the range of YOC’s caused by the different phases. As expected, the YOC decreases with increasing ice roughness.

4. Combined Target Offset and Ice Roughness

The combined effects of target offset and ice roughness on cryogenic-DT implosion yields are studied in this subsection. Both pulse shapes shown in Figs. 123.1(a) and 123.1(b) are simulated for ice roughnesses of $\sigma_{\text{rms}} = 1.0 \mu\text{m}$ and $\sigma_{\text{rms}} =$

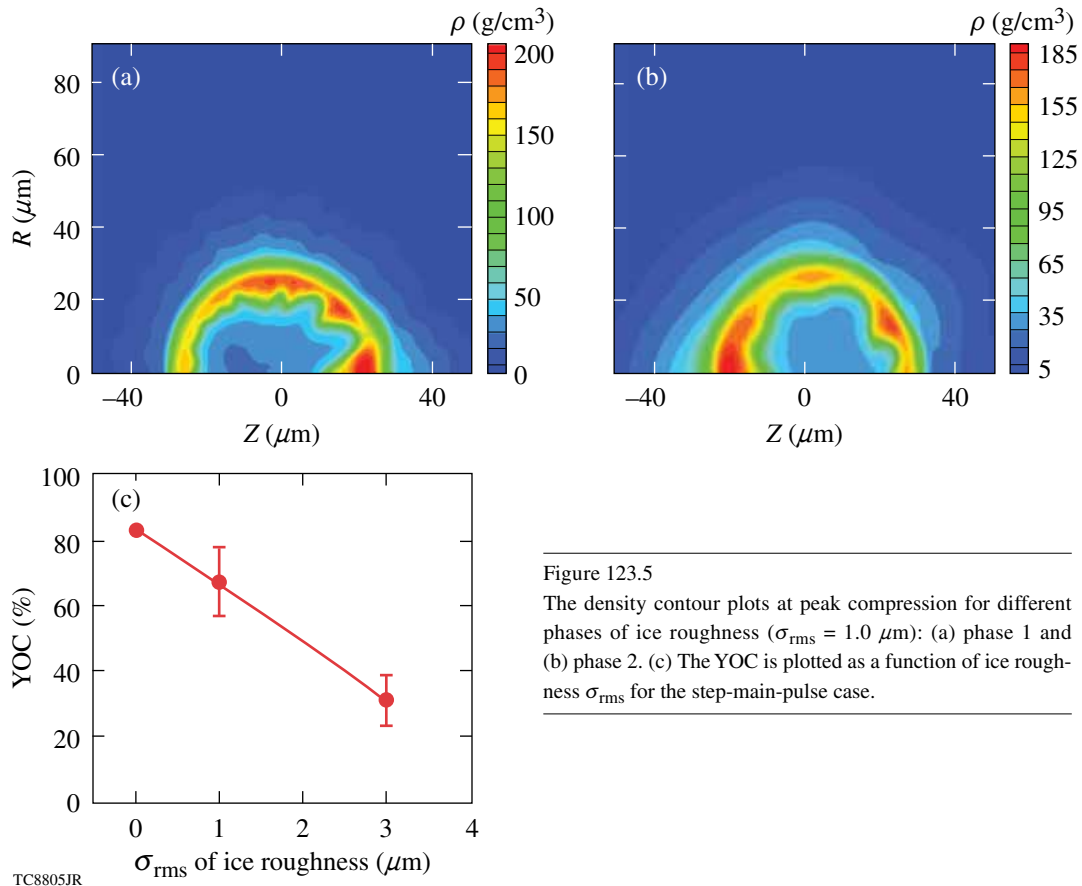


Figure 123.5
The density contour plots at peak compression for different phases of ice roughness ($\sigma_{\text{rms}} = 1.0 \mu\text{m}$): (a) phase 1 and (b) phase 2. (c) The YOC is plotted as a function of ice roughness σ_{rms} for the step-main-pulse case.

3.0 μm . The simulation results are shown in Figs. 123.6 and 123.7, respectively, by red circles (square main pulse) and blue squares (step main pulse). For the typical cryogenic-DT target ice roughness ($\sigma_{\text{rms}} = 1.0 \mu\text{m}$), Fig. 123.6 shows that the step main pulse resulted in more yield reduction than the square main pulse, again because of its lower adiabat and higher convergence. At an offset of about 20 μm , the square main pulse gives a factor-of-2-higher YOC than the step-main-pulse case, which is consistent with the experimental observation (discussed in *DRACO Simulations of Individual Cryogenic-DT Shots*, p. 122). A steeper drop in YOC is found for a target offset larger than 10 μm , especially for the step-main-pulse design, as illustrated in Fig. 123.6.

At a large ice roughness $\sigma_{\text{rms}} = 3.0 \mu\text{m}$, the YOC difference between the two pulse shapes is no longer significant since an increase in ice roughness dominates the performance and reduces the YOC to 30% to 40% (indicated by Fig. 123.7), even for target offsets $\leq 30 \mu\text{m}$. The step main pulse is more sensitive to the phase of the ice roughness, as indicated by the large YOC ranges in Fig. 123.7. To reach a high YOC level ($\geq 50\%$), the target must have a small offset ($\leq 10 \mu\text{m}$ for the step pulse

and $\leq 20 \mu\text{m}$ for the square pulse) and maintain a high-quality ice layer (ice roughness $\sigma_{\text{rms}} \leq 1 \mu\text{m}$).

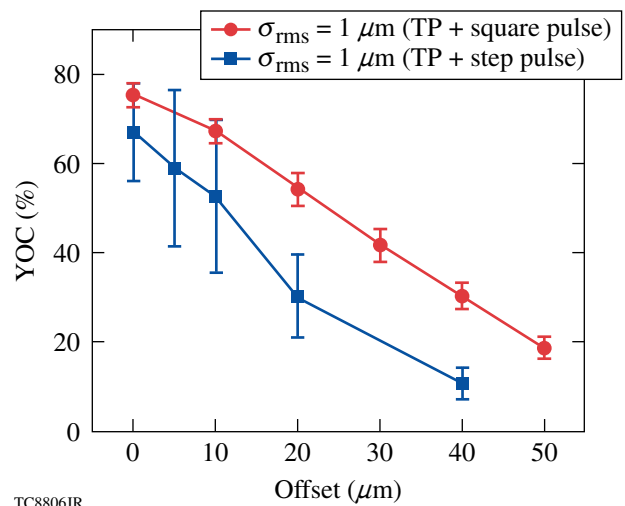


Figure 123.6
The YOC is plotted as a function of target offset with ice roughness $\sigma_{\text{rms}} = 1.0 \mu\text{m}$ for the two pulse shapes shown in Figs. 123.1(a) and 123.1(b).

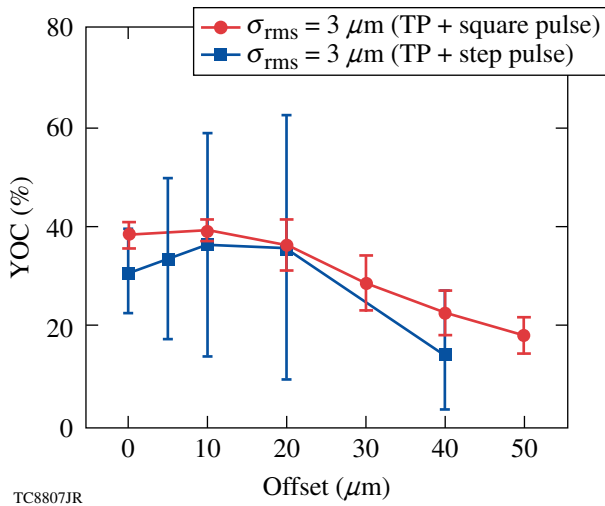


Figure 123.7

Same as Fig. 123.6 but for ice roughness $\sigma_{\text{rms}} = 3.0 \mu\text{m}$.

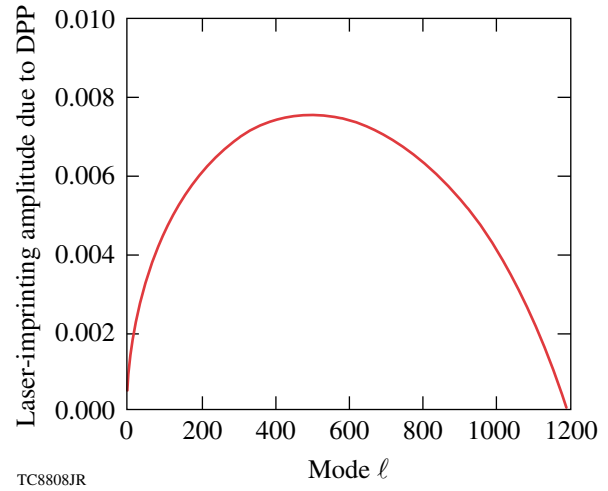


Figure 123.8

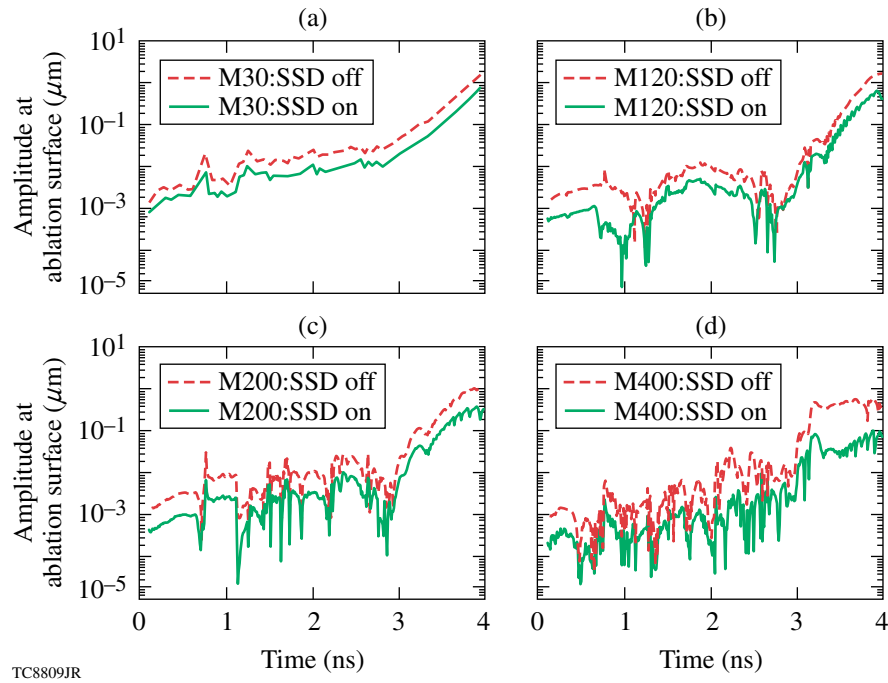
A typical SG-4 DPP spectrum on the OMEGA laser.

5. Laser Imprinting

Laser nonuniformities seed the instabilities at the ablation surface and can be categorized into long- and short-wavelength perturbations. The long-wavelength perturbations caused by beam mistiming, beam mispointing, and power imbalance have been discussed in **Long-Wavelength Laser Nonuniformities**, p. 113. The short-wavelength, single-beam nonuniformity caused by laser imprinting is addressed here.⁴⁰ An analytical model⁴¹ describing the nonuniformity of super-gaussian (SG) distributed phase plates (DPP's) is used to modulate the laser illumination on target. The experimentally confirmed SG-4 DPP spectrum⁴² is shown in Fig. 123.8. Polarization smoothing reduces the amplitudes by $\sqrt{2}$ (Ref. 34). Smoothing by spectral dispersion (1-THz, 2-D SSD) with one-color cycle⁴³ is applied for some shots. SSD is simulated using an analytical model.⁴⁴ The amplitudes of laser imprinting at the ablation surface are defined at the outer $1/e$ point of maximum density. These amplitudes seed the RT growth during the acceleration phase. Laser-imprinting effects are considered for both SSD-on and SSD-off cases.

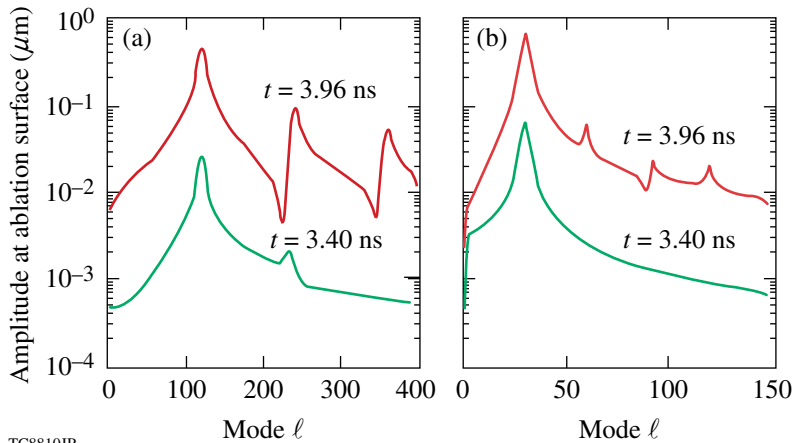
Single-mode laser-imprinting simulations for the step-main-pulse design up to mode $\ell = 500$ were performed with *DRACO* simulations either in a 45° wedge or in a half sphere. The resulting modulation amplitude at ablation surface is plotted as a function of time in Figs. 123.9(a)–123.9(d) for laser-imprinting modes $\ell = 30$ ($\lambda \approx 73.3 \mu\text{m}$), $\ell = 120$ ($\lambda \approx 18.3 \mu\text{m}$), $\ell = 200$ ($\lambda \approx 11.0 \mu\text{m}$), and $\ell = 400$ ($\lambda \approx 5.5 \mu\text{m}$), respectively.

The SSD-off cases are represented by dashed (red) curves and the SSD-on cases by solid (green) lines. For mode $\ell = 30$, Fig. 123.9(a) shows continuous imprinting before the start of acceleration at $t \approx 2.8$ ns. For modes $\ell \geq 120$, the laser imprinting decoupled during the first picket, when the distance from the laser deposition to the ablation surface became larger than the imprinting wavelength. The Richtmyer–Meshkov and preliminary RT growth caused by the unstable interference between the CD shell and the ice layer increase the amplitude. Phase reversals are seen in the high-mode laser-imprinting simulations, shown in Figs. 123.9(b)–123.9(d). After the acceleration starts at $t \approx 2.8$ ns, the $\ell = 30$ mode continuously grows until the end of acceleration ($t = 3.98$ ns), while the high modes of $\ell = 200$ and $\ell = 400$ quickly grow and nonlinearly saturate. The intermediate mode $\ell = 120$ grows linearly for about 600 ps; when its amplitude reaches $\sim 10\%$ of its wavelength, nonlinear behavior in RT growth begins. This can be seen in Fig. 123.10(a) where the Fourier transform of the single mode ($\ell = 120$) at the ablation surface (SSD on) is shown at two distinct times of $t = 3.4$ ns and $t = 3.96$ ns. At $t = 3.4$ ns, the $\ell = 120$ mode grows linearly, but at $t = 3.96$ ns, harmonics emerge as evidence of nonlinear growth.⁹ At the end of the acceleration phase, the shell radius converges to $R = 100 \mu\text{m}$ so that for the $\ell = 120$ mode, its wavelength is about $\sim 5 \mu\text{m}$, but $\lambda = 21 \mu\text{m}$ for a low mode $\ell = 30$. At $t = 3.96$ ns, the $\ell = 120$ mode grows to an amplitude of $\sim 0.8 \mu\text{m}$ [see Fig. 123.9(b)], which is $\sim 16\%$ of its wavelength. The mode $\ell = 120$ becomes nonlinear at the end of acceleration. For the low-mode $\ell = 30$



TC8809JR

Figure 123.9 The laser-imprinting mode growth as a function of time for both SSD-off and SSD-on cases from single-mode simulations: (a) $\ell = 30$, (b) $\ell = 120$, (c) $\ell = 200$, and (d) $\ell = 400$.



TC8810JR

Figure 123.10 The modal spectrum for our single-mode simulations (SSD on) at two distinct times $t = 3.40$ ns and $t = 3.96$ ns, for two cases (a) $\ell = 120$ and (b) $\ell = 30$.

case, the RT growth remained in a linear stage to the end of acceleration, which is confirmed by the absence of harmonics in Fig. 123.10(b).

By scanning the different single-mode simulations, the modulation amplitudes at the ablation surface as a function of laser-imprinting mode are shown in Figs. 123.11(a) and 123.11(b) at the start and end of acceleration, respectively. Both SSD-on (green squares) and SSD-off (red circles) cases

are shown in Fig. 123.11. The simulation results show that SSD reduces the modulation amplitude by a factor of 3 to 4, depending on the mode range. Overall, the laser-imprinting spectra (at the end of acceleration) show two distinct peaks around $\ell = 30$ and $\ell = 120$ for the triple-picket, step-main-pulse, cryogenic-DT design. The laser-imprinting spectra for the triple-picket design are compared with previous continuous-pulse, 5- μ m-CD-shell designs^{45,46} in Fig. 123.12(a) at the start of the acceleration phase and Fig. 123.12(b) at the end of the

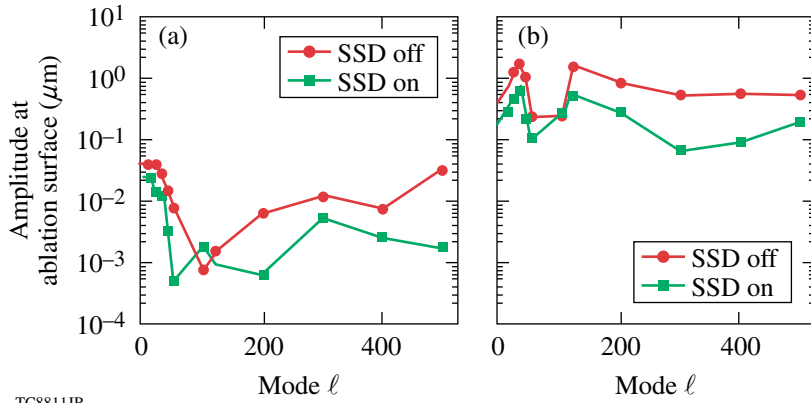


Figure 123.11

The laser-imprinting spectrum at (a) the start of acceleration and (b) the end of acceleration, for both SSD-off and SSD-on cases.

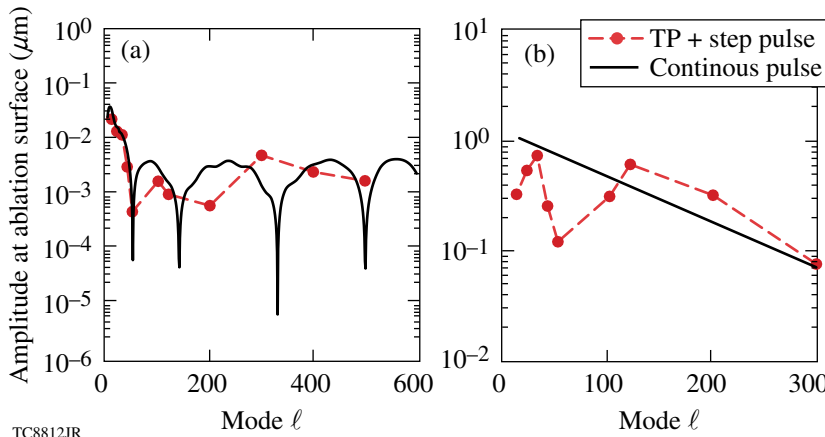


Figure 123.12

The laser-imprinting comparison between the triple-picket plus step-pulse (circles) and the continuous-pulse designs (solid lines) at (a) the start of acceleration and (b) the end of acceleration for the SSD-on case.

acceleration phase for the SSD-on case. The laser imprinting for the triple-picket design is comparable to the imprinting of the continuous-pulse and 5- μm -CD-shell designs, even though a 10- μm -thick CD shell was used in the triple-picket design (for the purpose of reducing potential fast-electron preheat⁴⁷). This is accomplished with the strong adiabat shaping^{46,48} caused by the three pickets.

The single-mode studies were performed up to a very high mode of $\ell = 500$, where there was evidence that short-wavelength (high-mode) RT growth can be stabilized in high-intensity drives at $I \sim 10^{15} \text{ W/cm}^2$ in planar experiments.^{11,12} At such high intensity, the corona temperature is about $T_e \approx 3 \text{ keV}$, resulting in a heat-carrying electron energy of around 15 to 20 keV. These electrons nonlocally affect the heat transport.^{29,49} They can penetrate to provide an extra heating at the ablation surface, which may in turn cause the ablation velocity to increase, leading to the short-wavelength RT stabilization, as the growth rate⁵⁰ scales as $\gamma - 0.94 \sqrt{kg / (1 + kL_m)} - 1.5 kV_a$, with wave number k , acceleration g , density scale length L_m , and ablation velocity V_a . Planar experiments with a wavelength

of $\lambda = 20 \mu\text{m}$ have shown no RT growth at such high-intensity drive conditions.^{11,12} For the cryogenic-DT, triple-picket designs, the laser intensity peaks at $I \sim 8 \times 10^{14} \text{ W/cm}^2$, which results in a corona temperature of $\sim 2.7 \text{ keV}$. Since the mean free path of the heat-carrying electrons scales with $\sim T_e^{-2}$, it is estimated that perturbations with $\lambda < 15$ to $16 \mu\text{m}$ should be stabilized, which corresponds to modes $\ell \geq 150$ to 200 (at the initial radius of $R = 350 \mu\text{m}$ at the start of acceleration). Therefore, for the multimode simulations the maximum mode was chosen to be $\ell_{\text{max}} = 200$. The multimode simulations were performed using a 45° wedge. To satisfy the boundary conditions, every fourth mode was included in the simulations. The amplitudes of the skipped ($\Delta \ell = 4$) modes were added in quadrature to conserve the total σ_{rms} of laser imprinting. Sixteen grid points per wavelength were used for the maximum laser-imprinting mode. The grid can support the harmonic growth of lower laser-imprinting modes ($\ell < 100$). The result of a simulation with $\ell_{\text{max}} = 200$ is shown in Fig. 123.13(a), where the density contours are plotted in the SSD-on case at the end of acceleration. It indicates two distinct features: (a) the dominant mode is around $\ell = 32$; (b) the second laser-

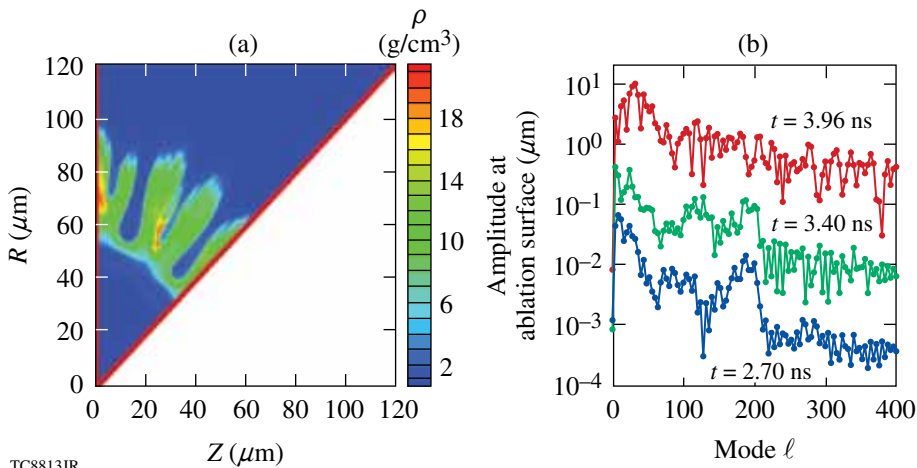


Figure 123.13
 (a) The density contour plot for a multimode simulation (up to mode $\ell_{\max} = 200$ with SSD on) at the end of acceleration; (b) the modal spectrum at different times for the same simulation.

imprinting peak is located around $\ell = 120$. Both features are consistent with the single-mode simulation results shown in Fig. 123.11(b). Figure 123.13(a) shows the “bubble” and “spike” growth, indicating the nonlinear growth and mode coupling.⁹ The Fourier transform of the ablation surface [Fig. 123.13(b)] shows the history of RT-growth modal spectra at times of $t = 2.7$ ns, $t = 3.4$ ns, and $t = 3.96$ ns. At $t = 2.7$ ns, the lower (blue) curve in Fig. 123.13(b) indicates a sharp cutoff at $\ell = 200$, the same as the maximum laser-imprinting seeds included. The modal spectra grow almost linearly to $t = 3.4$ ns with distinct features peaking at $\ell = 32$ and $\ell = 120$ beginning to appear. At the end of acceleration, the two overall peaks around $\ell = 32$ and $\ell = 120$ appear in the upper curve ($t = 3.96$ ns), which is consistent with the single-mode predictions. The nonlinear growth for imprinting modes $\ell = 100$ to 200 has washed out the mode cutoff around $\ell = 200$. Mode coupling caused by high-mode nonlinear growth enhances the low-mode growth that leads to effective disruption of the neutron production from the hot spot.

By including the maximum modes up to $\ell_{\max} = 50$, $\ell_{\max} = 100$, and $\ell_{\max} = 200$ separately in six multimode simulations, we obtained the laser-imprinting effects on the YOC. The results are shown in Fig. 123.14 for the step-main-pulse design in the SSD-on (red squares) and SSD-off (blue circles) cases. Figure 123.14 shows that simulations with multimodes up to $\ell_{\max} = 50$ hardly reduce the yield, even though the first imprinting peak around $\ell = 30$ has been included. This again indicates the laser imprinting to the yield-reduction effect is through the enhanced low-mode growth that is “fed” by the high-mode nonlinear saturation. High modes $\ell > 150$ may be stabilized by nonlocal electron heating of the ablation surface. This effect was not included in the *DRACO* simulations; therefore, the $\ell_{\max} = 200$ results may overestimate the

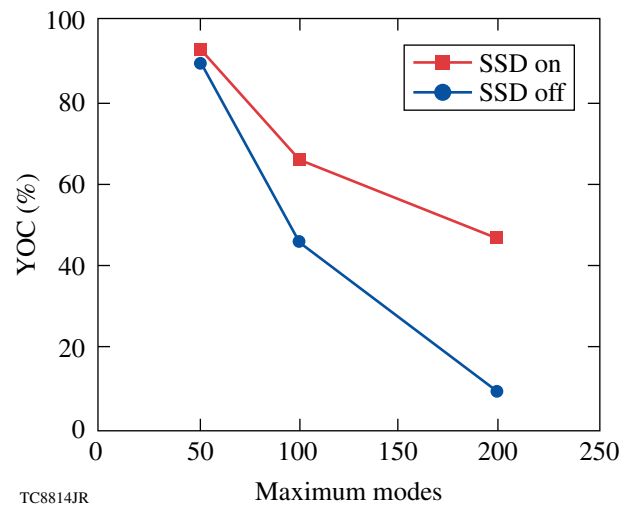


Figure 123.14
 The YOC is plotted as a function of maximum modes included in multimode simulations, for the step main pulse in SSD-off and SSD-on cases.

laser-imprinting effects. The multimode simulation up to about $\ell_{\max} = 150$ shows that the resultant YOC ratio of the SSD-on case to the SSD-off is ~ 2 . This agrees well with experimental observations that will be discussed in **DRACO Simulations of Individual Cryogenic-DT Shots**, p. 122. Laser-imprinting effects reduced the YOC to $\sim 50\%$ in the SSD-on case and further to $\sim 25\%$ in the SSD-off case. Turning on the SSD improved the yield by a factor of ~ 2 , which has been seen in both *DRACO* simulations and experiments.

Separate studies for each nonuniformity source (in the case of the step main pulse) have identified three dominant nonuniformities that affect the cryogenic-DT implosion performance: (a) a power imbalance ($\ell < 10$) of $\sim 10\%$ (pickets) and $\sim 3\%$ (main

pulse) reduce the YOC to $\sim 74\%$; (b) even with a high-quality ice layer ($\sigma_{\text{rms}} = 1 \mu\text{m}$), a target offset ($\ell = 1$) $> 20 \mu\text{m}$ reduces the YOC to $\sim 30\%$; and (c) the laser imprinting ($\ell = 20$ to 150) decreases the YOC to a level of $\sim 25\%$ (SSD off) and $\sim 50\%$ (SSD on). If these three major perturbation effects were taken as a product (assuming they behave independently in a different modal range), the yield would be about $\text{YOC} \simeq 5\%$ (SSD off) and $\text{YOC} \simeq 10\%$ (SSD on). This is in agreement (within a factor of ~ 2) with the measured YOC.

DRACO Simulations of Individual Cryogenic-DT Shots

A series of low-adiabat ($\alpha = 2.0$ to 2.5), cryogenic-DT target implosions have been performed using the triple-picket pulse designs [Figs. 123.1(a) and 123.1(b)] on OMEGA. Detailed compression dynamics and areal-density measurements up to $\langle \rho R \rangle \simeq 300 \text{ mg/cm}^2$ have been described in Refs. 17 and 18. Integrated DRACO simulations for nine individual cryogenic-DT shots that resulted in a large, absolute areal density of $\langle \rho R \rangle > 180 \text{ mg/cm}^2$ ($> 80\%$ of their 1-D designs) have been performed, including the actual experimental laser and target conditions. Low-mode ($\ell \leq 50$) DRACO simulations included the long-wavelength laser nonuniformities, target offset, and ice roughness (high-mode laser imprinting was not included). The low-mode simulation results (blue squares) shown in Fig. 123.15(a) compare the simulated YOC with the experimental values (red symbols) versus the target offset. Three phases of ice roughness have been examined for each shot in the DRACO simulations. The nine experimental shots are divided into three laser conditions: (1) triple-picket plus square main pulse with SSD on (red diamonds); (2) triple-picket plus square main pulse

with SSD off (red triangles); and (3) triple-picket plus step main pulse with SSD off (red circles). Figure 123.15(a) shows that for those shots with an offset larger than $\sim 25 \mu\text{m}$, the low-mode DRACO predictions can explain the experimental YOC since the target offset together with ice roughness ($\sigma_{\text{rms}} = 1$ to $2 \mu\text{m}$) is the dominant perturbation source. The low-mode DRACO neutron-yield predictions at small offsets are generally higher, however, than the experimental observations, in which the laser imprinting dominates.

A full simulation including both the low-mode perturbations discussed above and the high-mode laser imprinting has been performed up to $\ell_{\text{max}} = 200$ for a shot with a $3\text{-}\mu\text{m}$ offset. The resultant YOC is shown by the orange square in Fig. 123.15(b). Compared to the low-mode modeling ($\ell < 50$), the high-mode simulation reduces the YOC by a factor of ~ 4 for this shot (SSD off). This is in agreement with the results presented in **Laser Imprinting**, p. 118. For other shots, the laser-imprinting effects were taken into account by “scaling” low-mode simulation results by either a factor of ~ 2 reduction in the case of SSD on or a factor of ~ 4 reduction in the case of SSD off. The resultant high-mode predictions shown in Fig. 123.15(b) are compared with experiments. The high-mode DRACO predictions with laser-imprinting effects now agree with experimental YOC within a factor of 2 or better for all shots. From Fig. 123.15(b), two distinct features can be seen: (a) the square-main-pulse shots with SSD on give an experimental YOC of $\sim 9\%$ (red diamonds), which is twice as high as that of the same pulse shape with SSD off (red triangles); (b) the three step-main-pulse shots (red circles) with SSD off

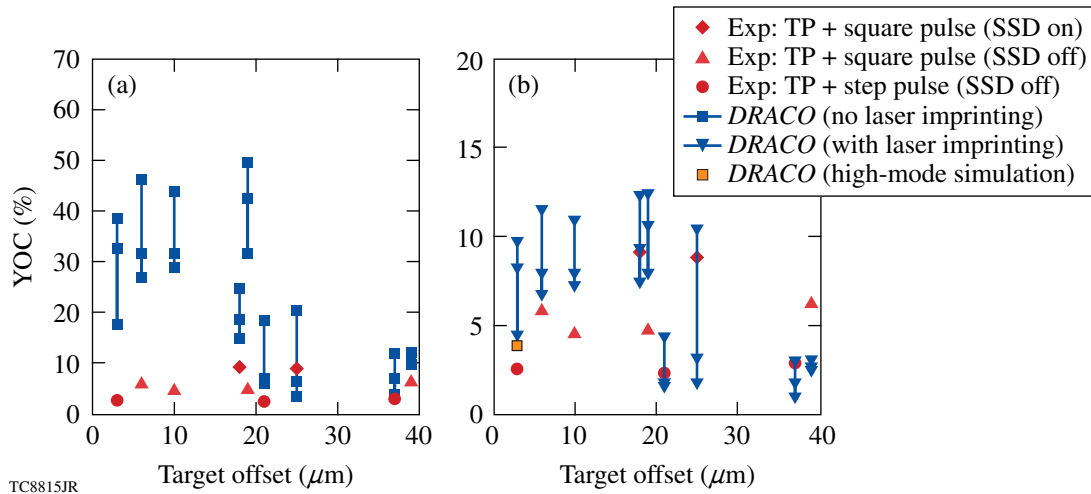


Figure 123.15

The YOC comparison between experiments and DRACO simulations for individual shots: (a) without laser imprinting and (b) with laser imprinting considered.

have a YOC level of 2% to 3%, which is a factor of 2 below the square main pulse (red triangles) with SSD off. All of these behaviors are well reproduced by the *DRACO* simulations (see also Figs. 123.6 and 123.14).

The simulated ion temperatures for these individual shots are compared with experimental measurements in Fig. 123.16. In experiments, the neutron-averaged ion temperature $\langle T_i \rangle$ is inferred by neutron time-of-flight spectroscopy.²² The measurement uncertainty is about ± 0.5 keV, shown in Fig. 123.16. The simulated $\langle T_i \rangle$ for each shot has three entries based on the phases examined. To take into account laser-imprinting effects, the high-mode scaling of $\langle T_i \rangle$ was done by either 10% or 15% reduction to the low-mode simulated $\langle T_i \rangle$, respectively, to the shots with SSD on and SSD off, as has been seen in the direct high-mode simulations. Figure 123.16 indicates that the *DRACO*-simulated $\langle T_i \rangle$ agrees with measurements within the experimental error bars. The TOC is defined as the ratio of experimental or *DRACO*-simulated $\langle T_i \rangle$ to its 1-D–designed value, e.g., $\text{TOC} = \langle T_i \rangle_{\text{exp or 2-D}} / \langle T_i \rangle_{1\text{-D}}$. The YOC versus TOC for all the shots is shown in Fig. 123.17. The experimental points are represented by red circles and the *DRACO* simulations by blue squares. The *DRACO* simulations tracked the experimental trend very well. The experimental error bar and simulation range of TOC are shown. A fitting line, $\text{YOC} \simeq 0.25 \times (\text{TOC})^4$, just passes through both experimental and simulated points for the SSD-off shots. For the cryogenic-DT implosion conditions, the neutron yield N is proportional to the hot-spot volume (V), density (ρ), ion temperature (T_i), and the burn time (t_b) as

$$N \propto V \times t_b \times \rho^2 \times T_i^4. \quad (2)$$

If Eq. (2) is divided by the 1-D clean values on each side, it gives

$$\text{YOC} = \left[\frac{\rho \sqrt{V t_b}}{(\rho \sqrt{V t_b})_{1\text{-D}}} \right]^2 \times (\text{TOC})^4. \quad (3)$$

The prefactor “0.25” of the solid green fitting line in Fig. 123.17 means that the product of hot-spot density and the square root of its volume and burn time reduced to $\sim 50\%$ of its 1-D value. This fitting characterizes the hot-spot distortion. The two shots with SSD on are above the fitting line. To have a fitting line with the same format passing through these two points, the prefactor is roughly about 0.49, meaning less hot-spot distortion (i.e., the product of hot-spot density and the square root of its volume

and burn time has been reduced to $\sim 70\%$ of its 1-D value when SSD is turned on). The dashed red fitting line for the SSD-on case plotted in Fig. 123.17 confirms the importance of SSD for these implosions.

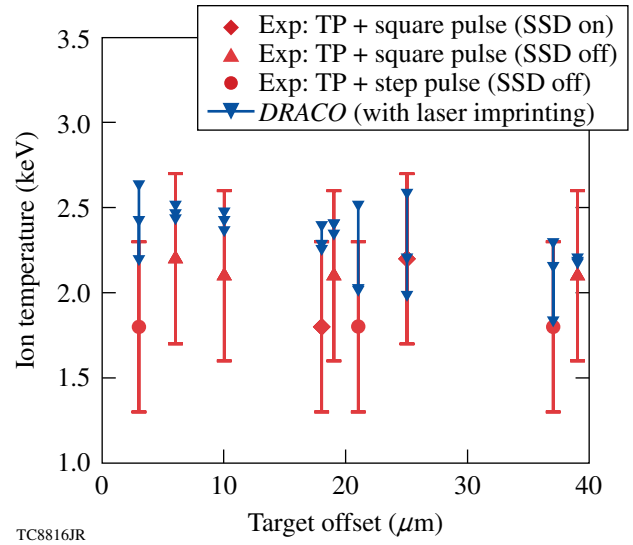


Figure 123.16 The neutron-averaged ion temperature comparison between experiments and *DRACO* simulations (with laser imprinting) for individual shots.

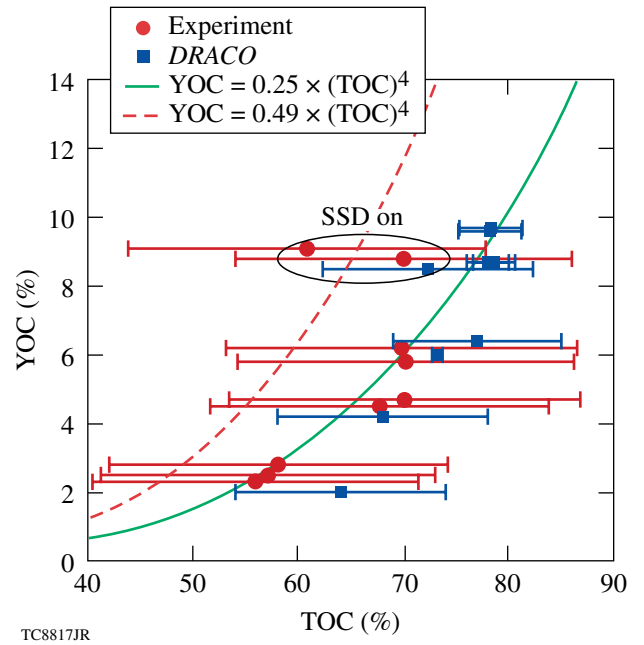


Figure 123.17 The relationship between YOC and TOC indicates the distortion of the hot-spot volume and density.

To have an insight into the hot-spot distortion caused by different perturbations, we calculated the clean volume fraction (CVF) and the volume-weighted surface area at the peak neutron-production time for different perturbed cases. The CVF is defined as the ratio of perturbed volume within the $T_i = 3$ -keV contour to the uniform case, i.e., $CVF = V(T_i > 3 \text{ keV}) / V_{1-D}(T_i > 3 \text{ keV})$. The surface area (A) along the $T_i = 3$ -keV contour can also be calculated from the simulations. Since the heat conduction loss is proportional to the surface area, we define the volume-weighted surface-area increase factor (SAIF) to be $SAIF = (A/V) / (A/V)_{1-D}$. In Fig. 123.18, we plot the YOC as a function of CVF and SAIF for (a) different target offsets of 40 μm , 20 μm , 10 μm , and 5 μm , and (b) the laser-imprinting effect. Figure 123.18(a)

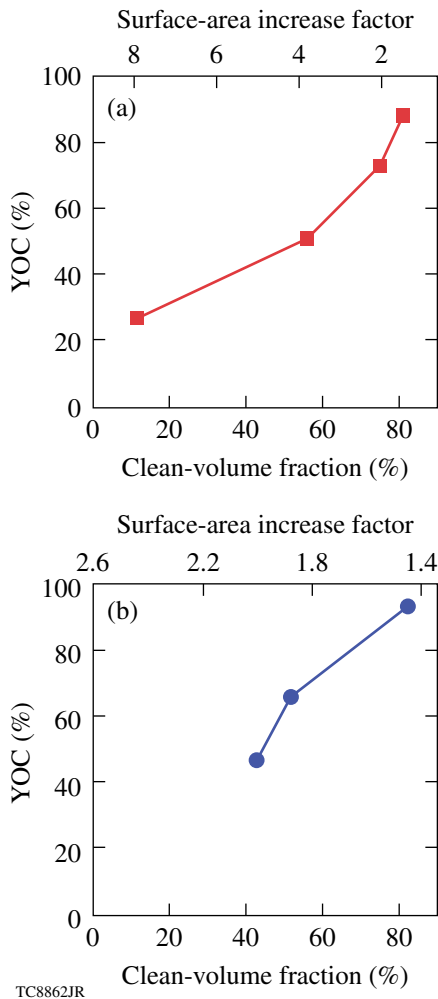


Figure 123.18 YOC as a function of the clean-volume fraction and the hot-spot surface-area-increase factor for (a) the target-offset effect and (b) the laser-imprinting effect (with step-pulse design).

shows that as the target offset increases, the CVF decreases and the volume-weighted surface area increases, leading to a smaller effective volume for neutron production and more heat loss. Therefore, when the target offset increases, the YOC becomes smaller and smaller, as does the neutron burn width. A similar analysis was also carried out for the laser-imprinting effect. The results, plotted in Fig. 123.18(b), show the different maximum modes ($\ell_{\text{max}} = 50, 100, \text{ and } 200$) included in the SSD-on simulations (same as Fig. 123.14). When more modes were included, the clean volume fraction decreased and the surface area increased, resulting in a decrease in YOC. We noticed that the target offset did not change the peak neutron-production time, while the laser imprinting caused peak neutron production earlier than in the uniform case. This was caused by the laser imprinting inducing “spikes” that pinched into the hot spot to increase the hot-spot pressure so that the shell tended to stagnate earlier. These analyses indicate that the major perturbations of both the target offset and laser imprinting cause a reduction in hot-spot volume and an increase in hot-spot surface area (leading to quick hot-spot cooling), which ultimately lead to neutron-yield reduction.

The areal density inferred from 2-D simulations is discussed briefly here; detailed discussions were presented in Ref. 18. Using the 2-D simulations, the down-scattered neutron spectrum from which the areal density $\langle \rho R \rangle$ is inferred was calculated. An example is shown in Fig. 123.19, where the blue diamonds indicate the angle-averaged $\langle \rho R \rangle$ expected from 2-D simulations, which compare to the 1-D–designed value represented by the dashed red line. This is for the square-main-pulse case with the offset-only perturbation. The $\langle \rho R \rangle$ range

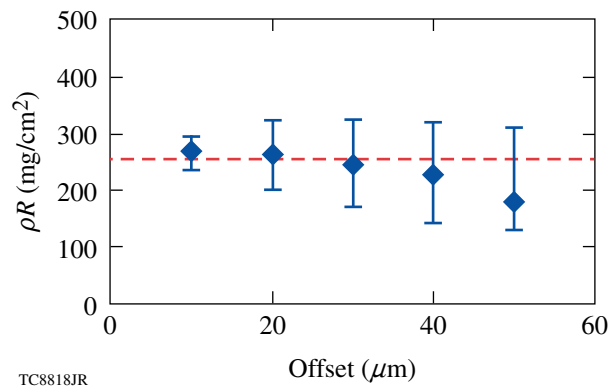


Figure 123.19 The areal density ($\langle \rho R \rangle$) inferred from the down-scattered neutron spectrum is plotted against the target offset. The dashed red line represents the corresponding 1-D value of $\langle \rho R \rangle$.

(error bar) is due to the different viewing angles around the target. Figure 123.19 indicates that the angle-averaged $\langle \rho R \rangle$ agrees with its 1-D–designed value if the offset is less than $20 \mu\text{m}$. The angle-dependent range of $\langle \rho R \rangle$ is within the MRS measurement uncertainty of $\pm 20\%$. Examinations of other perturbation sources show that the $\langle \rho R \rangle$ variation caused by perturbations is within the MRS measurement uncertainty.

Conclusions

In summary, the neutron-yield performance caused by a variety of nonuniformity sources for the cryogenic-DT implosions on OMEGA has been systematically investigated. The experimental trends are well-reproduced by 2-D *DRACO* hydrodynamic simulations: the simulated YOC agrees with experiments within a factor of 2 or better and the simulated ion temperatures $\langle T_i \rangle$ fall within the experimental uncertainty of measurements. The relationship between YOC and TOC provides an indication of how much the hot-spot volume, density, and burn time are reduced. Based on the simulations, two dominant nonuniformity sources have been identified: the target offset and laser imprinting, which mainly account for the yield reduction in the cryogenic-DT shots. Another important issue is the laser power imbalance during the pickets, which has now been improved to 3% to 4% from the previous $\sim 10\%$. The simulations suggest that to increase the YOC to an ignition-scaled level of $\sim 15\%$ to 20% for the step-main-pulse design (maintaining high-compression $\langle \rho R \rangle = 200$ to 300 mg/cm^2), the target offset must be $\leq 10 \mu\text{m}$ and SSD must be used.

ACKNOWLEDGMENT

This work was supported by the U.S. Department of Energy (DOE) Office of Inertial Confinement Fusion under Cooperative Agreement No. DE-FC52-08NA28302, the University of Rochester, and the New York State Energy Research and Development Authority.

REFERENCES

1. S. Atzeni and J. Meyer-ter-Vehn, *The Physics of Inertial Fusion: Beam Plasma Interaction, Hydrodynamics, Hot Dense Matter*, International Series of Monographs on Physics (Clarendon Press, Oxford, 2004); J. D. Lindl, *Inertial Confinement Fusion: The Quest for Ignition and Energy Gain Using Indirect Drive* (Springer-Verlag, New York, 1998).
2. J. Nuckolls *et al.*, *Nature* **239**, 139 (1972).
3. R. L. McCrory, D. D. Meyerhofer, R. Betti, R. S. Craxton, J. A. Delettrez, D. H. Edgell, V. Yu Glebov, V. N. Goncharov, D. R. Harding, D. W. Jacobs-Perkins, J. P. Knauer, F. J. Marshall, P. W. McKenty, P. B. Radha, S. P. Regan, T. C. Sangster, W. Seka, R. W. Short, S. Skupsky, V. A. Smalyuk, J. M. Soures, C. Stoeckl, B. Yaakobi, D. Shvarts, J. A. Frenje, C. K. Li, R. D. Petrasso, and F. H. Séguin, *Phys. Plasmas* **15**, 055503 (2008).
4. J. D. Lindl, *Phys. Plasmas* **2**, 3933 (1995).
5. S. E. Bodner, *Phys. Rev. Lett.* **33**, 761 (1974); H. Takabe *et al.*, *Phys. Fluids* **28**, 3676 (1985); H. J. Kull and S. I. Anisimov, *Phys. Fluids* **29**, 2067 (1986); A. B. Bud'ko and M. A. Liberman, *Phys. Fluids B* **4**, 3499 (1992); V. V. Bychkov, S. M. Goldberg, and M. A. Liberman, *Phys. Plasmas* **1**, 2976 (1994); J. Sanz, *Phys. Rev. Lett.* **73**, 2700 (1994); J. G. Wouchuk and A. R. Piriz, *Phys. Plasmas* **2**, 493 (1995).
6. R. Betti, V. N. Goncharov, R. L. McCrory, P. Sorotokin, and C. P. Verdon, *Phys. Plasmas* **3**, 2122 (1996); V. N. Goncharov, P. McKenty, S. Skupsky, R. Betti, R. L. McCrory, and C. Cherfils-Clérouin, *Phys. Plasmas* **7**, 5118 (2000).
7. P. Y. Chang, R. Betti, B. K. Spears, K. S. Anderson, J. Edwards, M. Fatenejad, J. D. Lindl, R. L. McCrory, R. Nora, and D. Shvarts, *Phys. Rev. Lett.* **104**, 135002 (2010).
8. J. Paisner *et al.*, *Laser Focus World* **30**, 75 (1994); E. M. Campbell and W. J. Hogan, *Plasma Phys. Control. Fusion* **41**, B39 (1999).
9. S. W. Haan, *Phys. Rev. A* **39**, 5812 (1989); M. M. Marinak *et al.*, *Phys. Rev. Lett.* **80**, 4426 (1998).
10. B. A. Remington *et al.*, *Phys. Rev. Lett.* **73**, 545 (1994); K. S. Budil *et al.*, *Phys. Rev. Lett.* **76**, 4536 (1996); C. J. Pawley *et al.*, *Phys. Plasmas* **6**, 565 (1999); J. P. Knauer, K. Anderson, R. Betti, T. J. B. Collins, V. N. Goncharov, P. W. McKenty, D. D. Meyerhofer, P. B. Radha, S. P. Regan, T. C. Sangster, V. A. Smalyuk, J. A. Frenje, C. K. Li, R. D. Petrasso, and F. H. Séguin, *Phys. Plasmas* **12**, 056306 (2005); V. A. Smalyuk, O. Sadot, J. A. Delettrez, D. D. Meyerhofer, S. P. Regan, and T. C. Sangster, *Phys. Rev. Lett.* **95**, 215001 (2005); H. Azechi *et al.*, *Phys. Rev. Lett.* **98**, 045002 (2007).
11. V. A. Smalyuk, S. X. Hu, V. N. Goncharov, D. D. Meyerhofer, T. C. Sangster, D. Shvarts, C. Stoeckl, B. Yaakobi, J. A. Frenje, and R. D. Petrasso, *Phys. Rev. Lett.* **101**, 025002 (2008).
12. V. A. Smalyuk, S. X. Hu, V. N. Goncharov, D. D. Meyerhofer, T. C. Sangster, C. Stoeckl, and B. Yaakobi, *Phys. Plasmas* **15**, 082703 (2008).
13. V. A. Smalyuk, S. X. Hu, J. D. Hager, J. A. Delettrez, D. D. Meyerhofer, T. C. Sangster, and D. Shvarts, *Phys. Rev. Lett.* **103**, 105001 (2009).
14. V. A. Smalyuk, S. X. Hu, J. D. Hager, J. A. Delettrez, D. D. Meyerhofer, T. C. Sangster, and D. Shvarts, *Phys. Plasmas* **16**, 112701 (2009).
15. T. R. Boehly, D. L. Brown, R. S. Craxton, R. L. Keck, J. P. Knauer, J. H. Kelly, T. J. Kessler, S. A. Kumpan, S. J. Loucks, S. A. Letzring, F. J. Marshall, R. L. McCrory, S. F. B. Morse, W. Seka, J. M. Soures, and C. P. Verdon, *Opt. Commun.* **133**, 495 (1997).
16. S. X. Hu, P. B. Radha, J. A. Marozas, R. Betti, T. J. B. Collins, R. S. Craxton, J. A. Delettrez, D. H. Edgell, R. Epstein, V. N. Goncharov, I. V. Igumenshchev, F. J. Marshall, R. L. McCrory, D. D. Meyerhofer, S. P. Regan, T. C. Sangster, S. Skupsky, V. A. Smalyuk, Y. Elbaz, and D. Shvarts, *Phys. Plasmas* **16**, 112706 (2009).
17. V. N. Goncharov, T. C. Sangster, T. R. Boehly, S. X. Hu, I. V. Igumenshchev, F. J. Marshall, R. L. McCrory, D. D. Meyerhofer, P. B. Radha, W. Seka, S. Skupsky, C. Stoeckl, D. T. Casey, J. A. Frenje, and R. D. Petrasso, *Phys. Rev. Lett.* **104**, 165001 (2010).

18. T. C. Sangster, V. N. Goncharov, R. Betti, T. R. Boehly, D. T. Casey, T. J. B. Collins, R. S. Craxton, J. A. Delettrez, D. H. Edgell, R. Epstein, K. A. Fletcher, J. A. Frenje, V. Yu. Glebov, D. R. Harding, S. X. Hu, I. V. Igumenshchev, J. P. Knauer, S. J. Loucks, C. K. Li, J. A. Marozas, F. J. Marshall, R. L. McCrory, P. W. McKenty, D. D. Meyerhofer, P. M. Nilson, S. P. Padalino, R. D. Petrasso, P. B. Radha, S. P. Regan, F. H. Séguin, W. Seka, R. W. Short, D. Shvarts, S. Skupsky, V. A. Smalyuk, J. M. Soures, C. Stoeckl, W. Theobald, and B. Yaakobi, *Phys. Plasmas* **17**, 056312 (2010).
19. P. B. Radha, T. J. B. Collins, J. A. Delettrez, Y. Elbaz, R. Epstein, V. Yu. Glebov, V. N. Goncharov, R. L. Keck, J. P. Knauer, J. A. Marozas, F. J. Marshall, R. L. McCrory, P. W. McKenty, D. D. Meyerhofer, S. P. Regan, T. C. Sangster, W. Seka, D. Shvarts, S. Skupsky, Y. Srebro, and C. Stoeckl, *Phys. Plasmas* **12**, 056307 (2005); D. Keller, T. J. B. Collins, J. A. Delettrez, P. W. McKenty, P. B. Radha, B. Whitney, and G. A. Moses, *Bull. Am. Phys. Soc.* **44**, 37 (1999).
20. T. R. Boehly, D. H. Munro, P. M. Celliers, R. E. Olson, D. G. Hicks, V. N. Goncharov, G. W. Collins, H. F. Robey, S. X. Hu, J. A. Marozas, T. C. Sangster, O. L. Landen, and D. D. Meyerhofer, *Phys. Plasmas* **16**, 056302 (2009).
21. J. A. Frenje, K. M. Green, D. G. Hicks, C. K. Li, F. H. Séguin, R. D. Petrasso, T. C. Sangster, T. W. Phillips, V. Yu. Glebov, D. D. Meyerhofer, S. Roberts, J. M. Soures, C. Stoeckl, K. Fletcher, S. Padalino, and R. J. Leeper, *Rev. Sci. Instrum.* **72**, 854 (2001).
22. T. J. Murphy, R. E. Chrien, and K. A. Klare, *Rev. Sci. Instrum.* **68**, 610 (1997).
23. J. A. Marozas, F. J. Marshall, R. S. Craxton, I. V. Igumenshchev, S. Skupsky, M. J. Bonino, T. J. B. Collins, R. Epstein, V. Yu. Glebov, D. Jacobs-Perkins, J. P. Knauer, R. L. McCrory, P. W. McKenty, D. D. Meyerhofer, S. G. Noyes, P. B. Radha, T. C. Sangster, W. Seka, and V. A. Smalyuk, *Phys. Plasmas* **13**, 056311 (2006).
24. B. I. Bennett *et al.*, Los Alamos National Laboratory, Los Alamos, NM, Report LA-7130 (1978).
25. W. F. Huebner *et al.*, Los Alamos National Laboratory, Los Alamos, NM, Report LA-6760-M (1977).
26. R. C. Malone, R. L. McCrory, and R. L. Morse, *Phys. Rev. Lett.* **34**, 721 (1975).
27. S. P. Regan, R. Epstein, V. N. Goncharov, I. V. Igumenshchev, D. Li, P. B. Radha, H. Sawada, W. Seka, T. R. Boehly, J. A. Delettrez, O. V. Gotchev, J. P. Knauer, J. A. Marozas, F. J. Marshall, R. L. McCrory, P. W. McKenty, D. D. Meyerhofer, T. C. Sangster, D. Shvarts, S. Skupsky, V. A. Smalyuk, B. Yaakobi, and R. C. Mancini, *Phys. Plasmas* **14**, 056305 (2007).
28. T. R. Boehly, E. Vianello, J. E. Miller, R. S. Craxton, T. J. B. Collins, V. N. Goncharov, I. V. Igumenshchev, D. D. Meyerhofer, D. G. Hicks, P. M. Celliers, and G. W. Collins, *Phys. Plasmas* **13**, 056303 (2006).
29. S. X. Hu, V. Smalyuk, V. N. Goncharov, S. Skupsky, T. C. Sangster, D. D. Meyerhofer, and D. Shvarts, *Phys. Rev. Lett.* **101**, 055002 (2008).
30. V. N. Goncharov, O. V. Gotchev, E. Vianello, T. R. Boehly, J. P. Knauer, P. W. McKenty, P. B. Radha, S. P. Regan, T. C. Sangster, S. Skupsky, V. A. Smalyuk, R. Betti, R. L. McCrory, D. D. Meyerhofer, and C. Cherfils-Clérouin, *Phys. Plasmas* **13**, 012702 (2006).
31. S. X. Hu, V. A. Smalyuk, V. N. Goncharov, J. P. Knauer, P. B. Radha, I. V. Igumenshchev, J. A. Marozas, C. Stoeckl, B. Yaakobi, D. Shvarts, T. C. Sangster, P. W. McKenty, D. D. Meyerhofer, S. Skupsky, and R. L. McCrory, *Phys. Rev. Lett.* **100**, 185003 (2008).
32. I. V. Igumenshchev, F. J. Marshall, J. A. Marozas, V. A. Smalyuk, R. Epstein, V. N. Goncharov, T. J. B. Collins, T. C. Sangster, and S. Skupsky, *Phys. Plasmas* **16**, 082701 (2009).
33. Y. Lin, T. J. Kessler, and G. N. Lawrence, *Opt. Lett.* **20**, 764 (1995).
34. T. R. Boehly, V. A. Smalyuk, D. D. Meyerhofer, J. P. Knauer, D. K. Bradley, R. S. Craxton, M. J. Guardalben, S. Skupsky, and T. J. Kessler, *J. Appl. Phys.* **85**, 3444 (1999).
35. J. A. Frenje, C. K. Li, F. H. Séguin, D. T. Casey, R. D. Petrasso, T. C. Sangster, R. Betti, V. Yu. Glebov, and D. D. Meyerhofer, *Phys. Plasmas* **16**, 042704 (2009).
36. D. R. Harding, D. D. Meyerhofer, S. J. Loucks, L. D. Lund, R. Janezic, L. M. Elasky, T. H. Hinterman, D. H. Edgell, W. Seka, M. D. Wittman, R. Q. Gram, D. Jacobs-Perkins, R. Early, T. Duffy, and M. J. Bonino, *Phys. Plasmas* **13**, 056316 (2006).
37. T. C. Sangster, R. Betti, R. S. Craxton, J. A. Delettrez, D. H. Edgell, L. M. Elasky, V. Yu. Glebov, V. N. Goncharov, D. R. Harding, D. Jacobs-Perkins, R. Janezic, R. L. Keck, J. P. Knauer, S. J. Loucks, L. D. Lund, F. J. Marshall, R. L. McCrory, P. W. McKenty, D. D. Meyerhofer, P. B. Radha, S. P. Regan, W. Seka, W. T. Shmayda, S. Skupsky, V. A. Smalyuk, J. M. Soures, C. Stoeckl, B. Yaakobi, J. A. Frenje, C. K. Li, R. D. Petrasso, F. H. Séguin, J. D. Moody, J. A. Atherton, B. D. MacGowan, J. D. Kilkenny, T. P. Bernat, and D. S. Montgomery, *Phys. Plasmas* **14**, 058101 (2007).
38. J. A. Koch *et al.*, *Fusion Technol.* **38**, 123 (2000).
39. D. H. Edgell, W. Seka, R. S. Craxton, L. M. Elasky, D. R. Harding, R. L. Keck, and M. D. Wittman, *Fusion Sci. Technol.* **49**, 616 (2006).
40. V. N. Goncharov, S. Skupsky, T. R. Boehly, J. P. Knauer, P. McKenty, V. A. Smalyuk, R. P. J. Town, O. V. Gotchev, R. Betti, and D. D. Meyerhofer, *Phys. Plasmas* **7**, 2062 (2000).
41. R. Epstein, *J. Appl. Phys.* **82**, 2123 (1997).
42. S. P. Regan, J. A. Marozas, J. H. Kelly, T. R. Boehly, W. R. Donaldson, P. A. Jaanimagi, R. L. Keck, T. J. Kessler, D. D. Meyerhofer, W. Seka, S. Skupsky, and V. A. Smalyuk, *J. Opt. Soc. Am. B* **17**, 1483 (2000).
43. S. Skupsky, R. W. Short, T. Kessler, R. S. Craxton, S. Letzring, and J. M. Soures, *J. Appl. Phys.* **66**, 3456 (1989); J. E. Rothenberg, *J. Opt. Soc. Am. B* **14**, 1664 (1997).
44. J. A. Marozas, J. D. Zuegel, and T. J. B. Collins, *Bull. Am. Phys. Soc.* **54**, 306 (2009).
45. *LLE Review Quarterly Report* **82**, 49, Laboratory for Laser Energetics, University of Rochester, Rochester, NY, LLE Document No. DOE/SF/19460-344 (2000).
46. V. N. Goncharov, J. P. Knauer, P. W. McKenty, P. B. Radha, T. C. Sangster, S. Skupsky, R. Betti, R. L. McCrory, and D. D. Meyerhofer, *Phys. Plasmas* **10**, 1906 (2003).

47. V. A. Smalyuk, D. Shvarts, R. Betti, J. A. Delettrez, D. H. Edgell, V. Yu. Glebov, V. N. Goncharov, R. L. McCrory, D. D. Meyerhofer, P. B. Radha, S. P. Regan, T. C. Sangster, W. Seka, S. Skupsky, C. Stoeckl, B. Yaakobi, J. A. Frenje, C. K. Li, R. D. Petrasso, and F. H. Séguin, *Phys. Rev. Lett.* **100**, 185005 (2008).
48. K. Anderson and R. Betti, *Phys. Plasmas* **10**, 4448 (2003).
49. G. Schurtz *et al.*, *Phys. Rev. Lett.* **98**, 095002 (2007).
50. R. Betti, V. N. Goncharov, R. L. McCrory, and C. P. Verdon, *Phys. Plasmas* **5**, 1446 (1998).